Geomechanics and Engineering, *Vol. 37, No. 2 (2024) 179-187*
https://doi.org/10.12989/gae.2024.37.2.179

Dynamic evolution characteristics of water inrush during tunneling through fault fracture zone

Jian-hua Wang[a], Xing Wan, Cong Mou* and Jian-wen Ding

Transportation College, Southeast University, Nanjing 210096, China

(*Received May 29, 2022, Revised March 23, 2024, Accepted April 4, 2024*)

Abstract. In this paper, a unified time-dependent constitutive model of Darcy flow and non-Darcy flow is proposed. The influencing factors of flow velocity are discussed, which demonstrates that permeability coefficient is the most significant factor. Based on this, the dynamic evolution characteristics of water inrush during tunneling through fault fracture zone is analyzed under the constant permeability coefficient condition (CPCC). It indicates that the curves of flow velocity and hydrostatic pressure can be divided into typical three stages: approximate high-velocity zone inside the fault fracture zone, velocity-rising zone near the tunnel excavation face and attenuation-low velocity zone in the tunnel. Furthermore, given the variation of permeability coefficient of the fault fracture zone with depth and time, the dynamic evolution of water flow in the fault fracture zone under the variable permeability coefficient condition (VPCC) is also studied. The results show that the time-related factor (α) affects the dynamic evolution distribution of flow velocity with time, the depth-related factor (A) is the key factor to the dynamic evolution of hydrostatic pressure.

Keywords: constant permeability coefficient condition; dynamic evolution characteristics; fault fractured zone; unified time-dependent constitutive model; variable permeability coefficient condition; water inrush

1. Introduction

Fault fracture zone is commonly encountered during the tunnel construction which behaves as a conductive channel (Hwang and Lu 2007, Aalianvari *et al*. 2017, Li *et al*. 2019, Shahbazi *et al*. 2021, Song *et al*. 2021). The hydrological and geological environment will be changed nearby when the tunnel passes through the fault fractured zone (Baghbadorani *et al*. 2021, Eftekhari and Aalianvari 2019). The groundwater in the fault fracture zone flows into the tunnel with the increase of hydraulic gradient, resulting in the water inrush disaster during the tunnelling. Therefore, the research on the evolution characteristics of water inrush is of great significance, which can provide early warning and effective guidance for treatment in practical engineering.

To judge the water flow pattern accurately is essential for understanding the dynamic evolution characteristics. Brinkman equation has been widely used to describe the water flow in the fault fracture zone (Brinkman 1949, Eduard *et al*. 2012, Golfier *et al*. 2015, Williamson *et al*. 2019). Given the closed and invisible water flow in the fault fracture zone, however, it remains to be verified whether the Brinkman flow can describe its flow accurately. Meanwhile, Brinkman flow equation incorporates none time factor term, which fails to describe the dynamic evolution laws of water flow with time (Kolymbas *et al*. 2007, Shi *et al*. 2018). As reported, the permeability coefficient of fault fracture determines the flow pattern of groundwater, and the flow pattern tends to transform from Darcy to non-Darcy flow with the increase of permeability coefficient (Wang *et al*. 2012). Therefore, the general pattern of Darcy flow and non-Darcy flow by using permeability coefficient need to be discussed to replace a specific flow pattern (e.g., Brinkman flow) to describe the groundwater flow in the fault fracture zone.

In this paper, a unified time-dependent constitutive model is proposed to describe both Darcy and non-Darcy flow. Coupling the turbulence flow in the excavated tunnel, the spatial distribution of flow velocity and water pressure of the water inrush when the tunnel passes through the fault fracture zone under the constant permeability coefficient condition (CPCC) and the variable permeability coefficient condition (VPCC) are demonstrated. Thus, the dynamic evolution characteristics of water inrush during tunnelling through fault fracture zone is revealed.

2. Unified constitutive model of Darcy and Non-Darcy flow

2.1 Unified governing equation

To derive the governing equation for the unified constitutive model describing groundwater flow, the following assumptions are made: (1) The fault fracture zone is treated as an equivalent continuous medium, with groundwater uniformly distributed within it; (2) For Darcy flow, hydraulic conductivity is solely dependent on porosity

*Corresponding author, Ph.D. Student
E-mail: congmou@seu.edu.cn
[a]Ph.D.
E-mail: jianhua_wang@seu.edu.cn

ISSN: 2005-307X (Print), 2092-6219 (Online)

and fluid properties. However, for non-Darcy flow, the permeability coefficient varies and is correlated with the hydraulic gradient.

According to the equivalent continuum seepage principle, the governing equation of Darcy flow of groundwater in the aquifer is presented in Eq. (1) (Giese *et al*. 2018).

$$\frac{\partial(K\frac{\partial H}{\partial x})}{\partial x}+\frac{\partial(K\frac{\partial H}{\partial y})}{\partial y}=S_s\frac{\partial H}{\partial t} \tag{1}$$

where K denotes the permeability coefficient, H represents the hydraulic head, S_S is the storage coefficient ratio of aquifer.

The Forchheimer quadratic relationship between the hydraulic gradient and the seepage velocity is considered more appropriate for non-Darcy flow in the fault fracture zone (Wang *et al*. 2012, Shi *et al*. 2018, Ovalle-Villamil and Sasanakul 2019), as expressed in Eq. (2). At low flow velocities, the first term (the Darcy flow term) predominates, resulting in linear flow. Conversely, at high flow velocities, the second term assumes precedence, leading to non-linear flow behavior.

$$J=\frac{\mu}{\rho g k}v+\frac{\beta}{g}v^2 \tag{2}$$

where J is the hydraulic gradient, μ is the dynamic viscosity, k is the permeability, g is the gravity coefficient, v is the flow velocity, β is the non-Darcy flow influence coefficient.

To analyze Darcy and non-Darcy flow in a unified framework, the permeability coefficient is assumed as a variable parameter, which is correlated with the hydraulic gradient in non-Darcy flow. Darcy flow and non-Darcy flow are expressed in a unified form of $v = K(J)\,J$, Eq. (2) can be transformed into Eq. (3).

$$v=\left\{-\frac{\mu}{2k\rho\beta}+\left[(\frac{\mu}{2k\rho\beta})^2+\frac{g}{\beta}J\right]^{\frac{1}{2}}\right\}J^{-1}*J \tag{3}$$

Wang *et al*. (2012) proposed that the relationship between k and β could be determined by the smooth parallel plate tests, which was described as

$$\beta=0.0003k^{-0.6134} \tag{4}$$

According to Eqs. (3) and (4), the governing equation of unsteady non-Darcy flow can be deduced as shown in Eq. (5). It should be noted that when the groundwater flow conforms to Darcy flow, the permeability coefficient in the governing equation does not change with the hydraulic gradient，$K=k*\rho g/\mu$.

$$\frac{\partial(K(J)\frac{\partial H}{\partial x})}{\partial x}+\frac{\partial(K(J)\frac{\partial H}{\partial y})}{\partial y}=S_s\frac{\partial H}{\partial t} \tag{5}$$

$$K(J)=J^{-1}\left\{-\frac{\mu}{2k\rho\beta}+\left[(\frac{\mu}{2k\rho\beta})^2+\frac{g}{\beta}J\right]^{\frac{1}{2}}\right\} \tag{6}$$

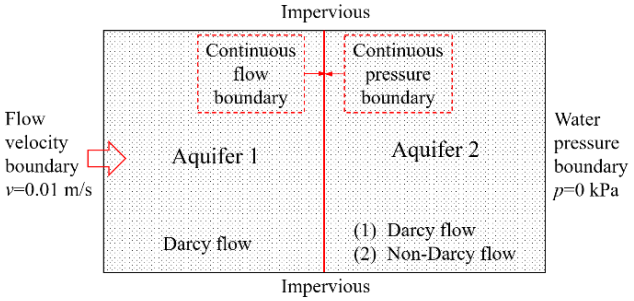

Fig. 1 The two-dimensional non-Darcy model

where K is the permeability coefficient of fault fracture zone, H represents the hydraulic head in the fault fracture zone, J is the hydraulic gradient, S_S is the storage coefficient ratio of fault fracture zone.

2.2 Differences between non-Darcy flow and Darcy flow

In order to illustrate the differences between non-Darcy flow and Darcy flow, a two-dimensional model is established, as shown in Fig. 1. The model, including aquifer 1 and aquifer 2, has a length of 30 m and a width of 6 m. The initial hydraulic head of the two aquifers are 30 m. The left end of aquifer 1 is the constant velocity boundary with a normal flow velocity of 0.01 m/s. The right end of aquifer 1 is the continuous flow and pressure boundary, which is consistent with the left end of aquifer 2. Furthermore, the right end of aquifer 2 is the atmospheric pressure boundary, and the relative pressure is 0. The upper and lower boundaries of aquifers 1 and 2 are impervious. In addition, the two aquifer has the constant hydraulic conductivity throughout the domains, the permeability coefficient of both aquifers is 1×10^{-4} m/s.

The numerical calculation schemes are as follows: aquifer 1 and 2 take the unsteady Darcy flow as the control equation in scheme 1; and in scheme 2, aquifer 1 takes the unsteady Darcy flow as the governing equation. and aquifer 2 takes the non-Darcy unsteady flow as the governing equation. The differences between Darcy flow and non-Darcy flow are analyzed with the same permeability coefficient. As for non-Darcy flow, the permeability coefficient changes obviously with the hydraulic gradient. That is, Eq. (5) is highly non-linear and does not have a general solution for the corresponding boundary conditions and initial conditions. Therefore, the finite-element (FE) solver in the PDE module of COMSOL Multiphysics, a commercial FE software, is used to solve Eq. (5).

As shown in Fig. 2, the flow velocity and hydrostatic pressure always increase with time. The increasing rate decreases gradually, which tends to be stable. Fig. 2(a) shows that the flow velocity distribution of non-Darcy flow is significantly higher than that of Darcy flow in aquifer 2, indicating that the seepage resistance of non-Darcy flow is smaller than that of Darcy flow even with the same permeability. As shown in Fig. 2(b), the hydrostatic pressure distribution of non-Darcy flow is significantly smaller than that than that of Darcy flow in aquifer 2, The

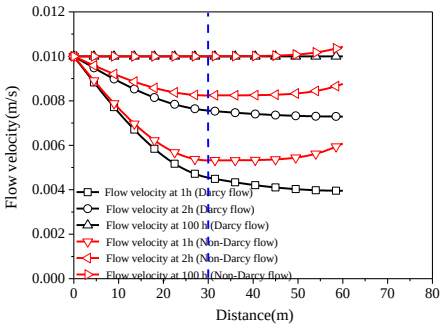

(a) Flow velocity dynamic evolution curves

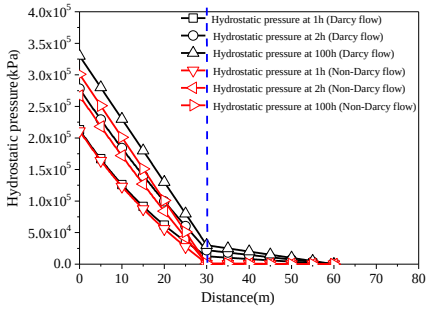

(b) Hydrostatic pressure dynamic evolution curves

Fig. 2 The differences between Darcy flow and non-Darcy flow

hydrostatic pressure drop of non-Darcy flow is greater than that of Darcy flow in the same area. In addition, the dynamic evolution of non- Darcy flow tends to be stable before Darcy flow.

Thus, the proposed governing equation of Darcy and non-Darcy flow can well describe the dynamic variation laws under the different flow patterns. The variation laws of flow velocity and hydrostatic pressure of non-Darcy flow conform the of high-velocity flow characteristics using this unified constitutive model (Shi *et al*. 2018). Next, the unified constitutive model of Darcy and non-Darcy will be used to describe the dynamic evolution characteristics of water inrush during tunneling through the fault fracture zone.

3. Numerical model for the water inrush during tunneling through fault fracture zone

3.1 The numerical modelling

The two-dimensional numerical model is developed (Khoei *et al*. 2020, Shiau and Al-Asadi 2020), which is based on a typical water inrush case of tunnelling through fault fracture zone (Hwang *et al*. 2007), as shown in Fig.3. The fault fracture zone has a width (B) of 15 m and a dip angle (θ) of 78°. The permeability coefficient of recharge aquifer (K_1) is 1×10^{-5} m/s, and the water storage coefficient ratio of recharge aquifer (S_{S1}) is 1×10^{-4}. The permeability coefficient of fault fracture zone (K) is 1.2×10^{-4} m/s and the storage coefficient ratio (S_S) is 1×10^{-4} m/s. The initial hydraulic heads of the recharge aquifer and the fault

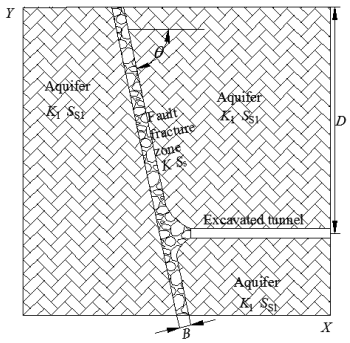

Fig. 3 The original model of water inrush

fracture zone are both 375 m (t=0, H_1=H=375 m). The drawdown at the tunnel heading (D) is 250 m. The equivalent continuum seepage method is adopted in the numerical model. Groundwater flow patterns in the recharge aquifer and fractured zone are defined as Darcy flow and non-Darcy flow, respectively. Groundwater in the excavated tunnel conforms to the Navier-Stokes turbulence flow.

The left and right boundaries (except for the tunnel excavation face), lower ends are considered as the impermeable boundaries ($\vec{n}K\nabla H=0$, $\vec{n}K_1\nabla H_1=0$). The upper boundaries of the model are considered as the constant head boundaries, H=H_1=375 m. The excavation face is the continuous boundary condition, which meets the continuous flux and pressure, as shown in Eq. (7).

$$nK_1\nabla H_1=-nK\nabla H \quad H_1=H \tag{7}$$

3.2 Scale effect of the recharge aquifer

The groundwater in the aquifer, around the fault fracture zone, supplies the fault fracture zone during the water inrush continuously. Thus, it is needed to discuss the effect of the aquifer size on the flow velocity. Fig. 4 shows the representative model with the different widths of the recharge aquifer, which includes the no aquifer model, shown in (a)), the original model (shown in (b)) and the aquifer increase 50 m model (shown in (c)). The parameters of all models are consistent with those of the original model shown in Fig. 3.

It can be seen from the Fig. 5 that the steady-state flow velocities are almost equal until the aquifer size increasing to 50 m. The steady-state flow velocities are at a lower level for the last three models (aquifer increase 100 m model, aquifer increase 150 m model, aquifer increase 350 m model), That is to say, there exists a range of aquifer size to keep flow velocity at a higher level. High flow velocities should be considered to take safe control measures in the practical engineering. Therefore, the original model adopted in this paper is more reasonable and meaningful.

3.3 The influence factors of water inrush

According to Eq. (2), Hwang *et al*. (2007) and Wang *et al*. (2012) pointed out that the flow velocity is subjected to

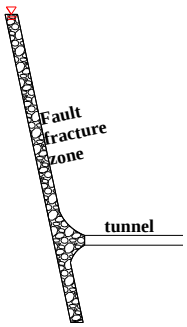

(a) No Aquifer model

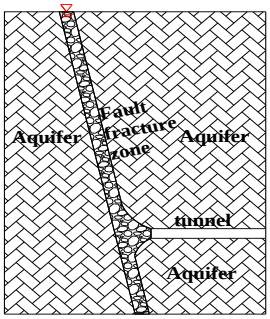

(b) The original model

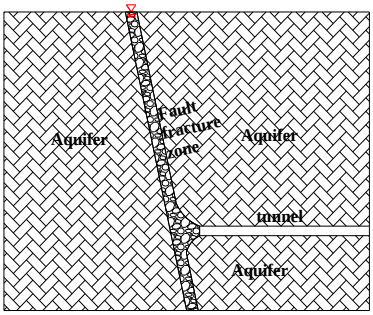

(c) Aquifer increase 50 m model

Fig. 4 Numerical models of different recharge aquifer sizes

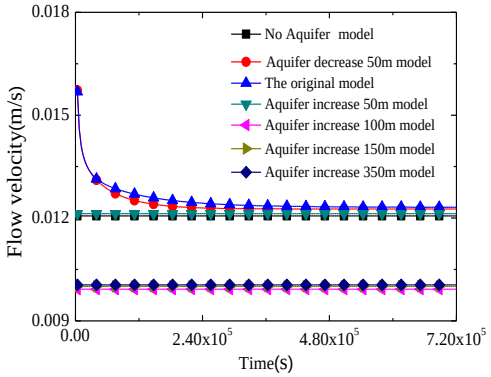

Fig. 5 Flow velocity curves with different aquifer sizes

the size of fault fracture zone (the dip angle θ, the fault width B), the storage coefficient ratio S_S, and the permeability coefficient K. The influence of these factors on the flow velocity should be discussed to acquire the main influencing factor.

Fig. 6 represents the curves of the flow velocity versus time for different influencing factors. As seen in Figs. 6(a)-(d), the flow velocity increases with the growing dip angle

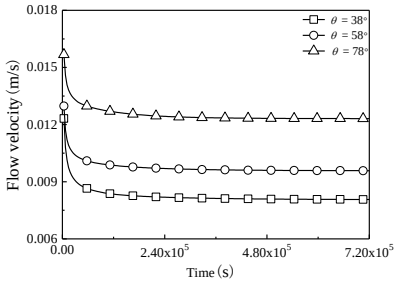

(a) Dip angle

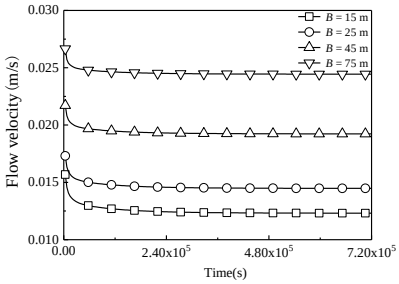

(b) Fault width

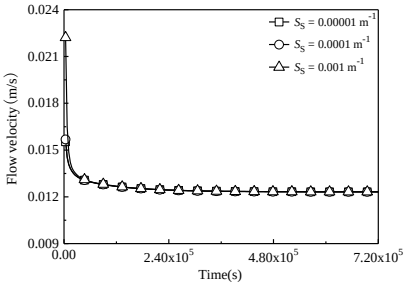

(c) Storage coefficient ratio

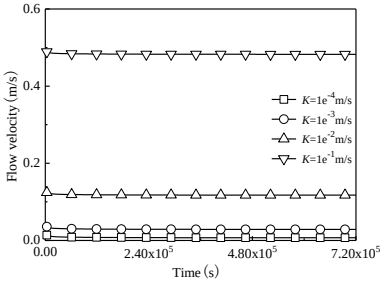

(d) Permeability coefficient

Fig. 6 Flow velocity curves under different influencing factors

and the fault width, but the influence of storage coefficient ratio on the flow velocity can be ignored. However, for a given size of fault fracture zone, the effect of the permeability coefficient on the flow velocity is more significant than storage coefficient ratio (Kim and Moon 2020). The larger permeability coefficient is, the greater the steady velocity will be.

4. Analysis of dynamic evolution characteristics

4.1 Dynamic evolution characteristics under CPCC

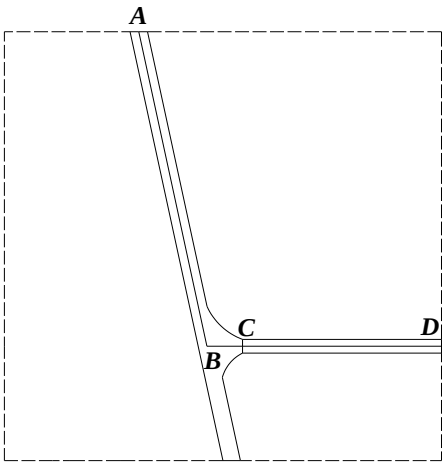

Fig. 7 The selected path of the water inrush model

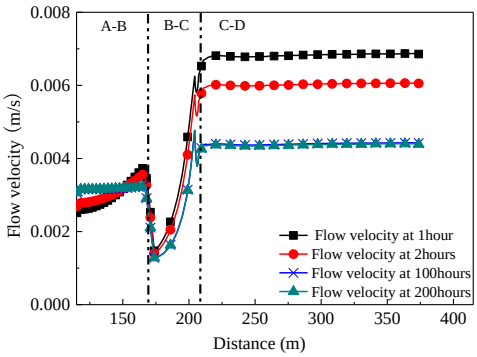

Fig. 8 Dynamic evolution of flow velocity under CPCC

To reveal the dynamic evolution characteristics of the water inrush during tunnelling through the fault fracture zone, a path A-B-C-D is selected, shown in the Fig. 7.

Fig. 8 gives the dynamic evolution laws of flow velocity at different locations in the fault fracture zone under CPCC. It can be seen from the figure that the curves can be divided into three stages. In the first stage (A-B), the flow velocity increases linearly with the increase of the horizontal distance. From Fig. 9, the flow velocity in *X* and *Y* direction increases almost linearly with the increase of the distance in this stage. It confirms that the flow pattern in this stage meets with the Darcy flow. In the second stage (B-C), the flow velocity increases rapidly with the increase of the horizontal distance. It should be attributed to the convergence of upstream and downstream water flow in the fault fracture zone. In the third stage (C-D), differently, the flow velocity is not sensitive to the horizontal distance.

Fig. 10 shows the dynamic evolution laws of hydrostatic pressure at different locations in the fault fracture zone under CPCC. It can be observed that the pressure firstly increases and then decreases with increasing horizontal distance in the first stage. In the second stage, the pressure decreases rapidly with horizontal distance. According to the Bernoulli's principle, such phenomenon occurs due to the decrease of the hydraulic head and the increase of the flow velocity. In the third stage, the hydrostatic pressure is almost constant and at a lower value.

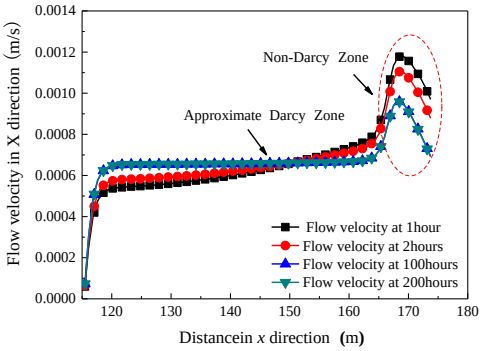

(a) in X direction

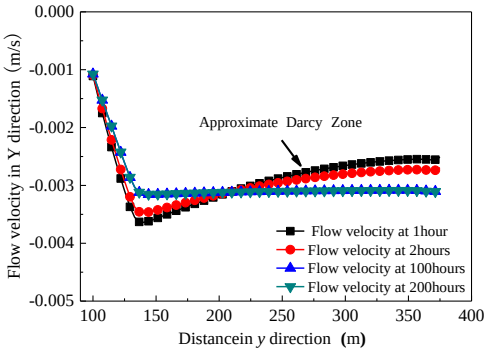

(b) in Y direction

Fig. 9 Dynamic evolution of flow velocity in X and Y directions

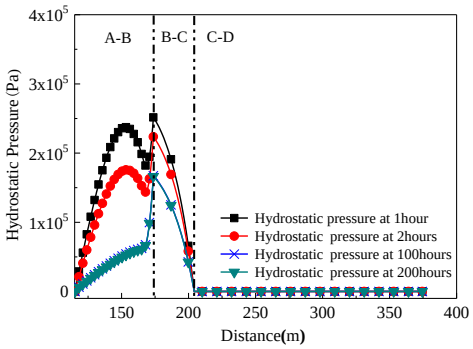

Fig. 10 Dynamic evolution of hydrostatic pressure under CPCC

4.2 Dynamic evolution characteristics under VPCC

The variable permeability coefficient mainly reflects that the permeability coefficient varies with depth and time in the fault fracture zone. On the one hand, it exhibits different permeability coefficients at different depths in the fault fracture zone (Jiang *et al.* 2009, Ameli *et al.* 2016, Rumynin *et al.* 2019). The permeability of a fault fracture zone is primarily influenced by stress levels and the degree of weathering, and decreases with the increase of buried depth. The variation in permeability coefficient along the depth of the fault fracture zone can be attributed to two

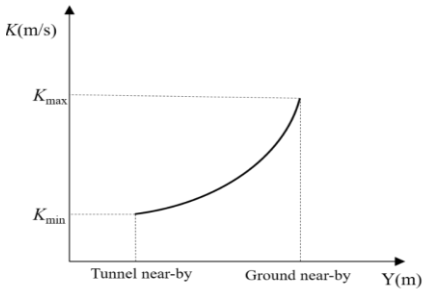

(a) Permeability coefficient varies with depth

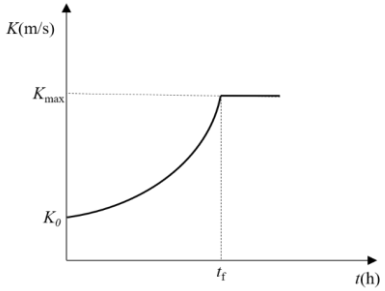

(b) Permeability coefficient varies with time

Fig. 11 Patterns of the variable permeability coefficient

main factors: (1) Changes in the fault fracture zone occur in response to varying stress levels at different buried depths. Higher stress levels lead to the closure of cracks, consequently reducing the permeability coefficient. (2) Rock masses deeply buried within the fault fracture zone tend to exhibit lower degrees of weathering, resulting in a lower permeability coefficient. Jiang *et al.* (2009) recommended exponential expression to describe the variation law of the permeability coefficient with depth, as shown in Fig. 11(a). The description can be expressed as

$$K_x(x,y) = K_y(x,y) = K_{\text{ground}}\left[-A(y_s(x) - y)\right] \tag{8}$$

where $K_x(x, y)$ and $K_y(x, y)$ are the components of the permeability coefficient K tensor, K_{ground} is the permeability coefficient at the ground surface, A is the depth-related factor, $y_s(x)$ is a function of the ground surface elevation.

On the other hand, the solid particles in the fault fracture zone will migrate and lose during the water inrush, resulting in continuous increase of the permeability of the fault fracture zone, as shown in Fig. 11(b). Yang *et al.* (2010) proposed the quantitative relationship of the permeability coefficient increasing with time, as shown in Eq. (9).

$$K = \begin{cases} K_0 \exp(\alpha t) & t \le t_f \\ K_{\max} & t > t_f \end{cases} \tag{9}$$

where K_0 is the initial permeability coefficient of the fault fractured zone, $K_{\max}$ is the maximum permeability coefficient of the fault fracture zone, α is the time-related factor. The greater α is, the more obvious the seepage erosion effect on the permeability will be. t_f is the time for the fully-developed water inrush channel in the fault fracture zone. when $t<t_f$, the process is that the permeability coefficient of water inrush channel increases gradually, when $t \ge t_f$, the permeability coefficient is a constant.

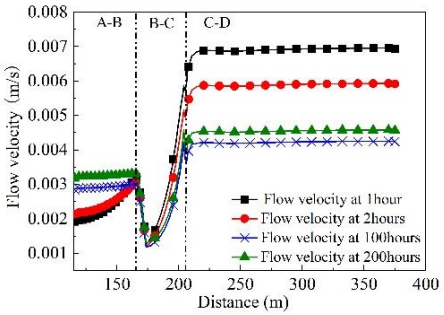

(a) A=0.002 m^{-1}, α = 0.04 d^{-1}

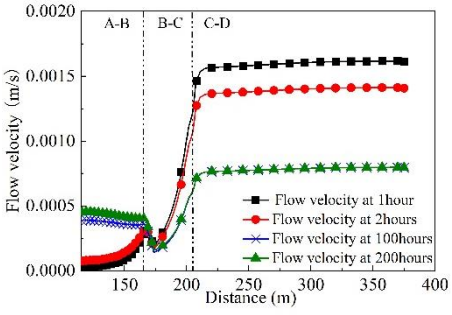

(b) A=0.02 m^{-1}, α = 0.04 d^{-1}

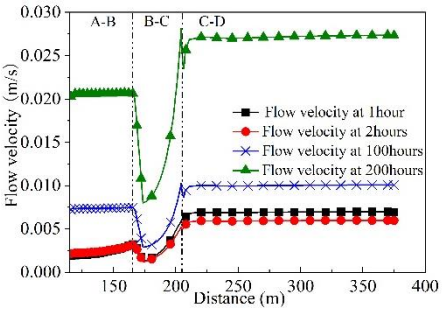

(c) A=0.002 m^{-1}, α = 0.4 d^{-1}

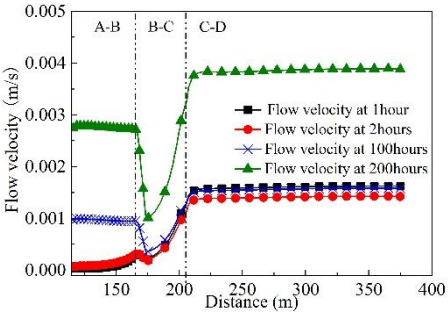

(d) A=0.02 m^{-1}, α = 0.4 d^{-1}

Fig. 12 Dynamic evolution of flow velocity under different A, α conditions

As the permeability coefficient is related to the depth and the time, the dynamic evolution characteristics of water inrush in the fault fracture zone under VPCC need to be discussed. In this study, the values of A and α are set as the different values. The corresponding results are shown in Figs. 12 and 13. As depicted in Fig. 12, both flow velocity and hydrostatic pressure are influenced by the time-related factor (α) and the depth-related factor (A), which govern changes in the permeability coefficient. Specifically, the time-related factor (α) and the depth-related factor (A) are

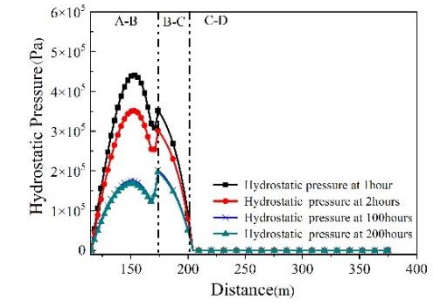

(a) A=0.002 m^{-1}, α = 0.04 d^{-1}

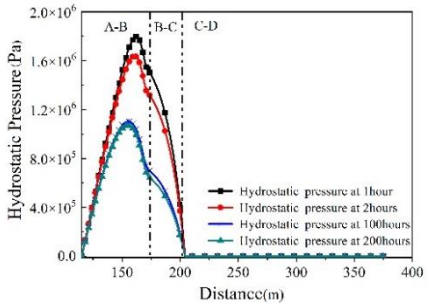

(b) A=0.02 m^{-1}, α = 0.04 d^{-1}

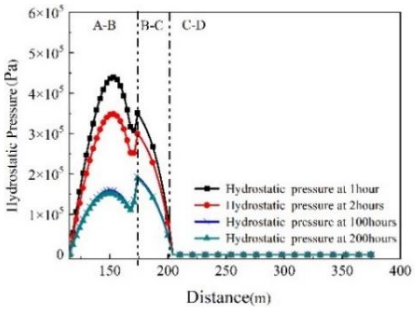

(c) A=0.002m^{-1}, α = 0.4 d^{-1}

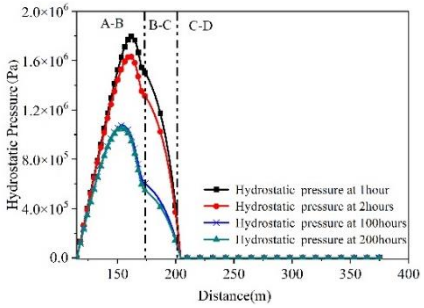

(d) A=0.02m^{-1}, α = 0.4 d^{-1}

Fig. 13 Dynamic evolution of hydrostatic pressure under different A, α conditions

the major effect factors. The depth-related factor (A) solely modulates the levels of flow velocity at different times. However, the time-related factor (α) exerts a more significant influence on flow velocity, capable of reshaping the dynamic evolution distribution characteristics of flow velocity over time. If the water inrush channel is formed slowly, the flow velocity in the tunnel gradually decreases to a lower level, as shown in Figs. 12(a) and 12(b). When the water inrush channel is still forming rapidly, the flow in the tunnel is always at a high velocity, as shown in Figs. 12(c) and 12(d). At this stage, the threat of water inrush disaster is the greatest.

From Fig. 13, the hydrostatic pressure gradually decreases during the water inrush under the different time-related factor (α) and depth-related factor (A). The influence of the depth-related factor (A) on the hydrostatic pressure should be considered, but the influence of the time-related factor (α) on the pressure can be ignored. Specifically, the depth-related factor (A) can significantly influence the hydraulic gradient, leading to notable changes in hydrostatic pressure. Conversely, the time-related factor (α) has a relatively minor impact on hydrostatic pressure. This is attributed to the higher hydraulic head within the fault fracture zone compared to the hydraulic head without considering the time-related factor (α), as the upper boundary maintains a constant hydraulic head. Additionally, the flow velocity experiences an increase when accounting for the time-related factor (α). However, according to the principles outlined in continuity and Bernoulli's equations, the equilibrium between the increase of both results in no significant change in hydrostatic pressure. The front of section B-C is the highest hydrostatic pressure area and is not an ideal location for the grouting treatment. should be considered, but the influence of the time-related factor (α) on the pressure can be ignored. Specifically, the depth-related factor (A) can significantly influence the hydraulic gradient, leading to notable changes in hydrostatic pressure. Conversely, the time-related factor (α) has a relatively minor impact on hydrostatic pressure. This is attributed to the higher hydraulic head within the fault fracture zone compared to the hydraulic head without considering the time-related factor (α), as the upper boundary maintains a constant hydraulic head. Additionally, the flow velocity experiences an increase when accounting for the time-related factor (α). However, according to the principles outlined in continuity and Bernoulli's equations, the equilibrium between the increase of both results in no significant change in hydrostatic pressure. The front of section B-C is the highest hydrostatic pressure area and is not an ideal location for the grouting treatment.

5. Conclusions

This paper analyzes the dynamic evolution characteristics of water inrush during tunnelling through a fault fracture zone using numerical methods. The main conclusions are as follows:

• A unified constitutive model of Darcy and non-Darcy flow is proposed. The governing equation of Darcy and non-Darcy flow accurately describes the dynamic variation laws under different flow patterns. The variation laws of flow velocity and hydrostatic pressure of non-Darcy flow conform to high-velocity flow characteristics.

• The dynamic evolution characteristics of water inrush under the CPCC is elaborated. The curves of flow velocity versus distance can be divided into three stages. In the first stage, flow velocity increases linearly with the horizontal distance, indicating approximate adherence to Darcy flow. In the second stage, flow velocity increases rapidly with horizontal distance. In the third stage, water flow becomes insensitive to horizontal distance.

• The dynamic evolution characteristics of the water inrush

in fault fracture zone under the VPCC is also studied. The time-related factor (α) alters the dynamic evolution distribution of flow velocity with time. Furthermore, the depth-related factor (A) emerges as the key determinant of hydrostatic pressure.

Acknowledgments

This work was supported by the International Postdoctoral Exchange Fellowship Program from China Postdoctoral Council (PC2021016). The authors would like to express appreciation to the reviewers for their valuable comments and suggestions that helped to improve the quality of the paper.

References

Aalianvari, A. (2017), "Combination of engineering geological data and numerical modeling results to classify the tunnel route based on the groundwater seepage", *Geomech. Eng.*, **13**(4), 671-683. https://doi.org/10.12989/gae.2017.13.4.671.

Ameli, A.A., McDonnell, J.J. and Bishop, K. (2016), "The exponential decline in saturated hydraulic conductivity with depth: a novel method for exploring its effect on water flow paths and transit time distribution", *Hydrol. Process*, **30**, 2438-2450. https://doi.org/10.1002/hyp.10777.

Baghbadorani, A.A., Hole, J.A., Baggett, J. and Ripepi, N. (2021), "Radar imaging of fractures and voids behind the walls of an underground mine", *Geophysics*, **86**(4), 27-41. https://doi.org/10.1190/GEO2020-0763.1.

Brinkman, H.C. (1949), "A calculation of the viscous force exerted by flowing fluid on a dense swam of particles", *Appl. Sci. Res.*, **1**(1), 27-34. https://doi.org/10.1007/BF02120313.

Eftekhari, A. and Aalianvari, A. (2019), "An overview of several techniques employed to overcome squeezing in mechanized tunnels; A case study", *Geomech. Eng.*, **18**(2), 215-224. https://doi.org/10.12989/gae.2019.18.2.215.

Giese, M., Reimann, T., Bailly-Comte, V., Marechal, J.C., Sauter, M. and Geyer, T. (2018), "Turbulent and laminar flow in karst conduits under unsteady flow conditions: interpretation of pumping tests by discrete conduit-continuum modeling", *Water Resour. Res.*, **54**(3), 1918-1933. https://doi.org/10.1002/2017WR020658.

Golfier, F., Lasseux, D. and Quintard, M. (2015), "Investigation of the effective permeability of vuggy or fractured porous media from a Darcy-Brinkman approach", *Computat. Geosci.*, **19**, 63-78. https://doi.org/10.1007/s10596-014-9448-5.

Hwang, J.H. and Lu, C.C. (2007), "A semi-analytical method for analyzing the tunnel water inflow", *Tunn. Undergr. Sp. Tech.*, **22**, 39-46. https://doi.org/10.1016/j.tust. 2006.03.003.

Jiang, X.W., Li, W., Wang, X.S., Ge, S.M. and Liu, J. (2009), "Effect of exponential decay in hydraulic conductivity with depth on regional groundwater flow", *Geophys. Res. Lett.*, **36**, L24402. https://doi.org/10.1029/2009GL041251.

Khoei, A.R., Sichani, A.S. and Hosseini, N. (2020), "Modeling of reactive acid transport in fractured porous media with the Extended-FEM based on Darcy-Brinkman-Forchheimer framework", *Comput. Geotech.*, **128**, 103778. https://doi.org/10.1016/j.compgeo.2020.103778.

Kim, Y. and Moon, J.S. (2020), "Change of groundwater inflow by cutoff grouting thickness and permeability coefficient", *Geomech. Eng.*, **21**(2), 165-170. https://doi.org/10.12989/gae.2020.21.2.165.

Kolymbas, D., and Wagner, P. (2007), "Groundwater ingress to tunnels-The exact analytical solution", *Tunn. Undergr. Sp. Tech.*, **22**(1), 23-27. https://doi.org/10.1016/j.tust.2006.02.001.

Li, S.C., Gao, C.L., Zhou, Z.Q., Li, L.P., Wang, M.X., Yuan, Y.C. and Wang, J. (2019), "Analysis on the precursor information of water inrush in karst tunnels: a true triaxial model test study", *Rock Mech. Rock Eng.*, **52**(2), 373-384. https://doi.org/10.1007/s00603-018-1582-2.

Ovalle-Villamil, W. and Sasanakul, l. (2019), "Investigation of non-Darcy flow for fine grained materials", *Geotech. Geol. Eng.*, **37**, 413-429. https://doi.org/10.1007/s10706-018-0620-x.

Rumynin, V.G., Leskova, P.G. and Nikulenkov, A.M. (2019), "Effect of depth-dependent hydraulic conductivity and anisotropy on transit time distributions", *J. Hydrol.*, **579**, 124161. https://doi.org/10.1016/j.jhydrol.2019.124161.

Shahbazi, A., Chesnaux, R. and Saeidi, A. (2021), "A new combined analytical-numerical method for evaluating the inflow rate into a tunnel excavated in a fractured rock mass", *Eng. Geol.*, **283**, 106003. https://doi.org/10.1016/j.enggeo.2021.106003.

Shi, W.H., Yang, T.H., Liu, H.L. and Yang, B. (2018), "Numerical modeling of non-Darcy flow behavior of groundwater outburst through fault using the Forchheimer equation", *J. Hydrol. Eng.*, **23**(2), 04017062. https://doi.org/10.1061/(ASCE)HE.1943-5584.0001617.

Shiau, J. and Al-Asadi, F. (2020), "Two-dimensional tunnel heading stability factors Fc, Fs and Fγ", *Tunn. Undergr. Sp. Tech.*, **97**, 103293. https://doi.org/10.1016/j.tust.2020.103293.

Song, Q., Xue, Y.G., Li, G.K., Su, M.X., Qiu, D.H., Kong, F.M. and Zhou, B.H. (2021), "Using Bayesian network and intuitionistic fuzzy analytic hierarchy process to assess the risk of water inrush from fault in subsea tunnel", *Geomech. Eng.*, **27**(6), 605-614. https://doi.org/10.12989/gae.2021.27.6.605.

Wang, Y., Qin, F., Xia, Z.H. and Ni, X.D. (2012), "Non-Darcy flow model and numerical simulation for prediction water inflow in deep tunnel", *Chin. J. Rock Mech. Eng.*, **31**(9), 1862-1868.

Williamson, K., Burda, P. and Sousedik, B. (2019), "A posteriori error estimates and adaptive mesh refinement for the Stokes-Brinkman problem", *Math. Comput. Simulat.*, **166**, 266-282. https://doi.org/10.1016/j.matcom.2019.05.015.

Yang, G.Y., Che, C.H. and Liu, S.C. (2010), "Numerical simulation of forecasting water inrush volume from fault", *J. Min. Saf. Eng.*, **27**(3), 351-355.

CC

List of symbols

A	depth-related factor
B	thickness of fault fracture zone
g	gravity coefficient
H	hydraulic head of fault fracture zone
K	permeability coefficient of fault fracture zone
K_0	initial permeability coefficient of fault fracture zone
K_{ground}	permeability coefficient at ground surface
K_{max}	maximum permeability coefficient of fault fracture zone
$K_x(x, y)$	component of the permeability coefficient K tensor in x direction
$K_y(x, y)$	component of the permeability coefficient K tensor in y direction
k	permeability
J	hydraulic gradient
S_S	storage coefficient ratio of fault fracture zone
S_{S1}	storage coefficient ratio of recharge aquifer
t_f	time for fully-developed water inrush channel in fault fracture zone
v	flow velocity
α	time-related factor
β	non-Darcy flow influencing coefficient
λ	hydraulic diffusivity of fault fracture zone
μ	dynamic viscosity
ρ	water density